

Velocity and density profiles of granular flow in channels using lattice gas automaton

Gongwen Peng^{*} and Takao Ohta[†]

Department of Physics, Ochanomizu University, Tokyo 112, Japan

May 3, 2018

Abstract

We have performed two-dimensional lattice-gas-automaton simulations of granular flow between two parallel planes. We find that the velocity profiles have non-parabolic distributions while simultaneously the density profiles are non-uniform. Under non-slip boundary conditions, deviation of velocity profiles from the parabolic form of newtonian fluids is found to be characterized solely by ratio of maximal velocity at the center to the average velocity, though the ratio depends on the model parameters in a complex manner. We also find that the maximal velocity (u_{max}) at the center is a linear function of the driving force (g) as $u_{max} = \alpha g - \delta$ with non-zero δ in contrast with newtonian fluids. Regarding density profiles, we observe that densities near the boundaries are higher than those in the center. The width of higher densities (above the average density) relative to the channel width is a decreasing function of a variable which scales with the driving force (g), energy dissipation parameter (ϵ) and the width of the system (L) as $g^\mu L^\nu / \epsilon$ with exponents $\mu = 1.4 \pm 0.1$ and $\nu = 0.5 \pm 0.1$. A phenomenological theory based on a scaling argument is presented to interpret these findings.

PACS numbers: 05.20.Dd, 47.50.+d, 47.20.-k, 46.10.+z

^{*}email: peng@phys.ocha.ac.jp

[†]email: ohta@phys.ocha.ac.jp

I. Introduction

Granular materials exhibit many interesting phenomena. The segregation of particles [1, 2, 3, 4], heap formation and convection cells under vibration [5, 6, 7, 8], and anomalous sound propagation [9] are just a few examples. Such phenomena occur because the dynamical responses of granular media are quite complex and different from those of usual solids, fluids and gases [10, 11, 12, 13, 14]. Considering the complexity in the dynamics, one is tempted to study first the granular materials in simple geometries and proceed then to more complicated situations. However, even in the simplest geometries such as hoppers and tubes, their flow under uniform external driving force (such as gravity) still shows complex dynamics [15, 16, 17, 18, 19, 20, 21]. For tubes, one can observe density waves in granular flow when the width of the tubes is narrow enough. Here the friction of the wall, as well as the dissipation among the grains themselves, plays an important role in the occurrence of density waves.

The purpose of this paper is to study granular flow in channels (different from tubes with wider width) and compare it with flow of Newtonian fluids. Comparison between granular flow and ordinary fluids is useful because it links with the knowledge that we have gained before. Besides the obvious contrast between the discreteness of granular materials and continuum of fluids, a key difference is that collisions of particles in granular flow are inelastic (energy-dissipative). In fluids, channel flow is a typical and fundamental topic in rheology (Poiseuille flow). Under the non-slip boundary conditions valid for viscous fluids, Newtonian fluids have a parabolic velocity profile across the channel. To claim that granular flow is non-Newtonian flow, a non-parabolic velocity profile is a clear and fundamental evidence. In this paper, we will report the non-parabolic shape of velocity profiles and non-uniformly distributed density profiles in granular channel flow.

Study on granular materials has a long history in engineering. Much engineering literature is devoted to understanding how to deal with these materials. However, it is only after the pioneering work of Bagnold [22] that theoretical work has begun to progress. Instead of focusing on the detailed dynamics of individual particles,

granular hydrodynamics [23, 24] treats the granular media like “fluids”. One defines a set of macroscopic quantities like particle density, velocity, and granular temperature. By assuming local equilibrium [25] one can write down the equations based on mass conservation, momentum conservation and energy balance. These equations are similar to the Navier–Stokes equations for fluids.

Using the idea of hydrodynamics, Savage [26] has studied the channel flow of cohesionless granular materials and obtained theoretically the velocity profiles. He obtained the velocity profiles under non-slip boundary conditions for different parameter R (which depends on the system parameters and on the density at the channel center). In the limiting case of $R = 0$ (which corresponds to the situation where density are uniformly distributed), the non-dimensional velocity profile has the form of $v = 1 - x^{3/2}$ where v is the velocity normalized to 1 with respect to the maximal velocity at the center, x is the distance from the channel center divided by the half-width of the channel. For larger R , the velocity profiles become more blunted (but without simple analytical form). Savage [26] performed also experiments to measure the velocity profile and found that his experiments corresponded to the case of $R = 0.3$. Since he did not intend to compare his results with those for fluids, his theory did not recover the parabolic velocity profile in any limiting case as he included from the beginning that the viscosity is proportional to the shear rate [22]. However, we find from his experimental data that the velocity is very close to have a parabolic shape.

In the following we will report our numerical results on the velocity profiles. We find that when the dissipation is very weak the velocity profiles are close to the parabolic shape while in the other cases they are more blunted than the parabolic form. As mentioned above, we realize that the key difference between fluids and granular flow is that the latter is energy dissipative. Therefore, when the parameter controlling the energy dissipation is switched off, the theory should recover that of fluids. Furthermore, we observe that density near the boundaries are higher than those at the channel center. Our numerical findings are consistent with the earlier experimental observations by Soo *et al* [27]: “the nature of the concentration, mass flow, and velocity distributions of solid particles is such that the concentration in-

creases toward the wall of the pipe, mass flow decreases toward the wall, and velocity is less than or equal to that of the stream at the core”.

In this paper we study the channel flow by computer simulations. Since a general theory for granular media is not yet available, people have used various computational methods to get better understanding about the complicated rheological behavior of granular media. Among the different methods are molecular dynamics (MD) [2, 18, 29, 30], Monte Carlo simulations [4, 31], the diffusing void model [32], event driven algorithms [33] and cellular automaton [34]. So far the most widely used method is MD [35] which simulates the granular materials on a “microscopic” level (the grain’s level). MD has been recognized to be very successful in simulating granular materials [36]. MD needs, however, much computer time to give reasonable results. To calculate the velocity and density profiles one needs long time average in order to get reasonable statistics.

The same situation was also faced in classical fluid mechanics some years ago when Frisch, Hasslacher and Pomeau [37] proposed lattice-gas automata (LGA) as a novel alternative to the direct solution of the equation of motion. As a sort of primitive molecular-dynamics system LGA offers the advantage of guaranteed numerical stability coupled with extreme computational simplicity. The basic idea behind LGA is that a properly defined cellular automaton with appropriate conservation laws should lead to the Navier-Stokes equations. A detailed comparison of simulational results from LGA and the well-established theory of Newtonian fluids in Poiseuille flow can be found in Refs. [38, 39]. The main check to the LGA for the Newtonian dynamics was the parabolic velocity profile in channel flows [38, 39, 40].

In this paper we employ the LGA model of Ref. [20] to study the velocity and density profiles in granular channel flow. The LGA of Ref. [20] is an extension of the LGA of usual fluids by including energy dissipation among the particles into the model. As emphasized above, energy dissipation is a major mechanism by which granular flow differs from ordinary fluids. The LGA models for granular materials were successful in simulating granular flow [20, 41, 42, 43].

This paper is organized as follows. We describe the model in some detail in Sect. II. The results obtained by simulations are presented in Sect. III. A phenomenological argument is made in Sect. IV to understand the numerical results. A discussion is contained in Sec. V.

II. Simulational model

We consider an LGA at integer time steps $t = 0, 1, 2, \dots$ with N particles located at the sites of a two-dimensional triangular lattice. The arrangement of the triangle lattice is depicted in Fig. 1 (a). At each site there are seven Boolean states which refer to the velocities, $\vec{c}_k (k = 0, 1, 2, \dots, 6)$. Here $\vec{c}_k (k = 1, 2, \dots, 6)$ are the nearest neighboring (NN) lattice vectors and $\vec{c}_0 = \vec{0}$ refers to the rest (zero velocity) state. Each state can be either empty or occupied by a single particle. Therefore, the number of particles per site has a maximal value of 7 and a minimal value of 0. In this paper we use the number of particles per site as density which can therefore be greater than 1.0. The time evolution of the LGA consists of a collision step and a propagation step. In the collision step particles change their velocities due to collisions and in the subsequent propagation step particles move in the directions of their velocities to the NN sites where they collide again.

The system is updated in parallel. Only the specified collisions shown in Fig. 1 can deviate the trajectories of particles. All collisions conserve mass and momentum.

For two- and three-body collisions, we have the probabilistic rules shown in Fig. 1 (b). The probability that a configuration may take place is shown next to the configuration. If the parameter ϵ is nonzero, it means that energy can be dissipated in the collision.

Collisions with rest particles may produce more than one rest particles on that site. This is allowed temporarily as in the Fig. 1 (c). However, immediately after the collision step, the extra rest particles randomly hop to NN sites until they find a site with no rest particle and there they stop.

We use no-slip boundary conditions at the channel walls which are parallel to the y -axis and periodic boundary conditions along the channel. No-slip conditions are employed by allowing that any particle colliding with the wall along any of the three possible directions bounces back into the incoming direction.

We incorporate the driving force, namely, gravity, in the way that Kadanoff *et al* [38] have used. The direction of gravity is along the y -axis, i.e., the downward in Fig. 1a. After each time step we randomly select a lattice site and, if possible, apply one of the forcing rules: (i) a rest particle goes into motion with equal probability along one of the two lattice directions which form an angle of 30° with the direction of gravity; (ii) a moving particle change its velocity by a unit vector along the direction of gravity if the resulting vector is possible on the triangle lattice used. Each successful application of a forcing rule adds one unit of momentum to the system. The forcing process is repeated until the desired amount of momentum (we label it as G) has been transferred to the system; fractional amounts of momentum to be added to the system are accumulated across time steps until they sum to an amount greater than 1, at which time one additional unit of momentum is added to the gas. The actual forcing scheme is slightly more complicated since it must compensate for inhomogeneity in the momentum and number densities due to the macroscopic flow (see also Ref. [38]). The forcing algorithm randomly selects a lattice row and column and then searches along that column until it finds a site where a forcing rule may be successfully applied. This guarantees that forcing operations will be uniformly distributed across the width of the channel, despite variations in the mass and momentum densities. It is noted that the magnitude of the gravity cannot be extremely large in our model system due to the following fact: on one hand the maximal velocity at the channel center increases with the increasing gravity, on the other hand the LGA only guarantees a velocity less than unit.

III. Simulation Results

We evolve the system according to the collision rules defined above. The initial configuration of the system is set to be random in the sense that every state (except the rest state) of each site is randomly occupied according to a preassigned average

density $\bar{\rho}$. We discard the configurations in the first period of several thousand time steps until we are sure that the system is in the steady state where energy input by gravity is averagely equal to the energy dissipation in the system. Fig. 2 shows a typical curve of the total kinetic energy relaxation starting from a random configuration at time step $t = 0$.

After the kinetic energy curve becomes flat, we then make the necessary average over space and time as follows. Let us label the particle number of state k ($k = 0, 1, 2, \dots, 6$) on the i th lattice site with coordinates (x_i, y_i) at time step t as $n_k(x_i, y_i, t)$. As depicted in Fig. 1(a), the x-coordinates of lattice sites take values of integers and half-integers of $0, 1/2, 1, \dots, L-1$, while the y-coordinates have values of $0, 1/2, 1, \dots, M-1$ with M even. The total number of lattice sites is $N = LM - M/2$. In this paper, we always keep $M = 2L$ and fix the average density $\bar{\rho} = 1.5$ unless otherwise specified.

We are interested in the density profile $\rho(x)$ and velocity profile in y-direction $u(x) = V_y(x)$ with x integer

$$\rho(x) = \frac{1}{2TM} \sum_{t=t_0+1}^{t_0+T} \sum_{i=1}^N \sum_{k=0}^6 n_k(x_i, y_i, t) \delta([x_i] - x) \quad (1)$$

$$u(x) = \frac{1}{2TM} \sum_{t=t_0+1}^{t_0+T} \sum_{i=1}^N \sum_{k=0}^6 c_k^{(2)} n_k(x_i, y_i, t) \delta([x_i] - x) \quad (2)$$

where the function $[z]$ takes the integer value of its variable z and function $\delta(z)$ equals to one when $z=0$ and zero otherwise. $\vec{c}_k = (c_k^{(1)}, c_k^{(2)}) = (\cos(\pi(k-1)/3), \sin(\pi(k-1)/3))$ for $(k = 1, 2, \dots, 6)$ are the unit vectors of the lattice bond orientation (and $\vec{c}_0 = \vec{0}$). We actually make average over two column whose x-coordinates have the same integer part, they are columns with x_i (integer) and $x_i + 1/2$ (half-integer), therefore, the normalization factor is $\frac{1}{2TM}$ where T is the time period over which we make average starting from time step t_0 . T is usually several tens of thousand time steps.

As a first step, we check that when the dissipation parameter ϵ is set to zero we recover the parabolic velocity profile of Newtonian fluids. This is shown in Fig. 3(a) for system size $L = 64$ with average density $\bar{\rho} = 1.8$. From Fig. 3(a) we can

estimate the magnitude of the kinematic viscosity equal to 0.35 according to Ref. [38]. Meanwhile, the density profile in Fig. 3(b) is just a flat curve, showing that density is uniformly distributed.

Fig. 4(a) and Fig. 4(b) show the velocity and density profiles when energy dissipation with $\epsilon = 0.01$ is present in the system. We see clearly that the parabolic velocity profile is no longer kept in this case, but more blunted. In fact, a parabolic curve demanding the maximum value at the center equal to the numerical data and zero at the two boundaries deviates substantially from the numerical data. It is also remarked that the density is not uniformly distributed, in contrast with those of Newtonian fluids.

Regarding the velocity profile, we can generally write down the following equation:

$$u(x) = u_{max}(\epsilon, g, L)\tilde{u}\left(\frac{x}{L}, \epsilon L^{\sigma_1}, gL^{\sigma_2}\right) \quad (3)$$

where u_{max} is the maximum velocity. Here gravity is taken to be system size independent quantity $g = G/N$ where G is the total amount of momentum added to the system after each time step and N is the total number of lattice sites.

A simple measure of the flatness of velocity profiles is the ratio $\gamma = u_{max}/\bar{u}$ where \bar{u} is the mean value of $u(x)$. It is equal to 1.5 for Poiseuille flow of Newtonian fluids and 1.0 for a perfectly flat profile. Note that γ can be written as

$$\gamma^{-1} = \int_0^1 \tilde{u}(x, \epsilon L^{\sigma_1}, gL^{\sigma_2}) dx \quad (4)$$

Fig. 5 displays the ratio γ versus gravity for two different dissipation parameters $\epsilon = 0.01$ and $\epsilon = 0.02$ with different channel widths. From Fig. 5 we see γ depends on the channel width, degree of dissipation and gravity. We find that γ can be solely used to characterize the shape function $\tilde{u}(x, \epsilon L^{\sigma_1}, gL^{\sigma_2})$. Taking two set of different parameters which leads to almost identical γ , e.g., $\{\epsilon_1 = 0.01, G_1 = 8.0, L_1 = 64\}$ and $\{\epsilon_2 = 0.02, G_2 = 10.0, L_2 = 48\}$ resulting $\gamma_1 = 1.27594$ and $\gamma_2 = 1.28298$, we show in Fig. 6 that their shape functions are almost identical. Note that both set of parameters $\{\epsilon, g, L\}$ share no common value but their resulting γ are almost identical. For comparison, the velocity profile for a different value of $\gamma = 1.35906$

is also plotted in Fig. 6. As expressed in Eq. (4), γ^{-1} is the 0th moment of the distribution function $\tilde{u}(x)$. Fig. 6 tells us that the distribution function \tilde{u} has such a property that as long as the 0th moment is determined higher order moments are determined. This may suggest that the parameters $\{\epsilon, g, L\}$ combine to give a scalar on which $\tilde{u}(x)$ depends solely.

In order to fit the velocity data, we have tried the polynomial fitting routines. We find that polynomial up to an order of 4 is not sufficient; most of the data can be fitted by a polynomial up to an order of 6:

$$\tilde{u}(x) = v_0 - v_2(x - c)^2 - v_4(x - c)^4 - v_6(x - c)^6 \quad (5)$$

where x is the normalized coordinate in the interval $[0:1]$ and c is the coordinate of the channel center. The three velocity profiles are fitted using Eq. (5) in Fig. 6. In the next section basing on a phenomenological theory we will propose a formula for velocity profiles where the dependences of these fitting parameters on the model parameters $\{\epsilon, g, L\}$ are clearly expressed and we will check our theory by the simulation data.

For $u_{max}(\epsilon, g, L)$, we find that it is a linear function of g as $u_{max}(\epsilon, g, L) = \alpha g - \delta$ with non-zero δ . Fig. 7 displays four curves of u_{max} for different channel widths but with fixed ϵ . The slope α depends on L but not as L^2 which is valid for Newtonian fluids. If we increase ϵ , the value of α decreases. Non-zero δ means that the driving force must exceed a non-zero threshold (δ/α) in order to drive the granular media into motion. From the statistics we are not sure whether δ is independent of L but one can see from Fig. 7 that the dependence is very weak, if any. Furthermore, although not shown in Figure, we find that δ have a tendency to approach zero as ϵ approaches zero, which recovers the case of Newtonian fluids.

Regarding the density profile, we observe that densities near the walls are higher than those at the channel center, in contrast to the uniform density distribution of Newtonian fluids. A simple way to characterize the spatial variation is to define a width over which densities are higher than the average density. We plot such a width (Δ) divided by channel width in Fig. 8 (a) against gravity g for different

system sizes and different dissipation parameters. Generally, Δ/L decreases with increasing g and increasing L but increases with increasing ϵ . The scattered data in Fig. 8(a) can be scaled to one curve as shown in Fig. 8 (b) where we plot Δ/L versus $g^\mu L^\nu/\epsilon$. We find that the exponents are $\mu = 1.4 \pm 0.1$ and $\nu = 0.5 \pm 0.1$.

We have checked that the above observations do not change their properties qualitatively as we change the average density $\bar{\rho}$. The scaling exponents μ and ν are independent of the average density.

IV. Phenomenological Theory

In this section we present a phenomenological theory to interpret our numerical findings. We note that there are two important system parameters, namely, g and ϵ : g is the velocity change per particle per time step and ϵ is energy dissipation per particle per time step. Therefore, using dimension analyse, we have

$$g = \frac{dV}{dt}, \quad \epsilon = \frac{dE}{dt}. \quad (6)$$

where V and E are characteristic velocity and kinetic energy of a particle. Hereinafter we put the particle's mass to be unity. Since $V^2 \sim E$, gV/ϵ must be dimensionless.

We may construct a quantity which has a dimension of velocity by using the channel width L as

$$V = \sqrt{gL} \quad (7)$$

The above argument implies that P defined as

$$P = \frac{gV}{\epsilon} = \frac{g^{3/2}L^{1/2}}{\epsilon} \quad (8)$$

must be a fundamental dimensionless quantity. Eq. (8) is consistent with the simulations illustrated in Fig. 8b where Δ/L is a function of a variable which scales as $g^\mu L^\nu/\epsilon$ with exponents $\mu = 1.4 \pm 0.1$ and $\nu = 0.5 \pm 0.1$.

Note that when $\epsilon = 0$, the system has another dimensionless quantity which can

be derived from the newtonian hydrodynamics equation

$$g + \nu \nabla^2 v = 0 \quad (9)$$

where $\nu = \mu/\rho$ is the kinematic viscosity. The two terms in Eq. (9) have the same dimension, therefore,

$$Q = \frac{gL^2}{\nu V} = \frac{gL^2}{\nu \sqrt{gL}} = \frac{g^{1/2} L^{3/2}}{\nu} \quad (10)$$

is another dimensionless quantity. Note in Eq. (10) we have used Eq. (7). Q is in fact the square root of the Reynolds number.

Now, we consider the maximum velocity u_{max} at the channel center. Simulations show that u_{max} is a linear function of g

$$u_{max} = \alpha g - \delta. \quad (11)$$

We determine the forms of α and δ . First of all, they do not depend on g by definition. Using Eq. (7), α must take the form

$$\alpha = \sqrt{\frac{L}{g}} \hat{\alpha}(P, Q) \quad (12)$$

The form of $\hat{\alpha}$ can be determined by the following conditions: (i) α (instead of $\hat{\alpha}$) is independent of g ; (ii) when $\epsilon \rightarrow 0$ ($P \rightarrow \infty$), $u_{max} = gL^2/\nu$. The simplest interpolation formula for $\hat{\alpha}$ is given by

$$\hat{\alpha} = \frac{1}{c_1 P^{-1/3} + c_2 Q^{-1}} \quad (13)$$

where c_1, c_2 are dimensionless positive numerical constants. In fact we have

$$\begin{aligned} \alpha g &= \sqrt{gL} \frac{1}{c_1 \left(\frac{\epsilon}{g^{3/2} L^{1/2}} \right)^{1/3} + c_2 \frac{\nu}{g^{1/2} L^{3/2}}} \\ &= \frac{g\sqrt{L}}{c_1 \left(\frac{\epsilon}{L^{1/2}} \right)^{1/3} + c_2 \frac{\nu}{L^{3/2}}} \end{aligned} \quad (14)$$

Therefore,

$$\alpha = \frac{L}{c_1 (\epsilon L)^{1/3} + c_2 \nu / L} \quad (15)$$

When $\epsilon = 0$, we recover the well-known result:

$$u_{max} \sim \frac{gL^2}{\nu} \quad (16)$$

When $\epsilon \rightarrow \infty$, Eq. (15) shows

$$\alpha = \frac{L^{2/3}}{c_1 \epsilon^{1/3}} \quad (17)$$

Our numerical results also show that α decreases with increasing ϵ , in the trend of Eq. (17). The $L^{2/3}$ is even reached in the simulations with $\epsilon = 0.02$. This is illustrated in Fig. 9. From Eq. (15) one may see that as long as ϵ is non-zero, the term with c_1 dominates the denominator for large L , leading to the validity of Eq. (17).

Now we determine δ . It should vanish at $\epsilon = 0$ and be independent of g for any non-zero value of ϵ . Using again the fact of Eq. (7) δ should be given by

$$\delta = c_3 \sqrt{gL} P^{-1/3} f(P/Q^3) = c_3 (\epsilon L)^{1/3} f(P/Q^3) \quad (18)$$

where c_3 is a positive constant. Note that $P/Q^3 = \nu^3/(\epsilon L^4)$ is independent of g . It seems that the form of $f(x)$ can not be specified phenomenologically. If we impose the fact that δ is insensitive to L as observed in simulations, $f(x)$ must be $f(x) \sim x^{1/12}$ so that we have

$$\delta = c_3 (\epsilon L)^{1/3} \nu^{1/4} \epsilon^{-1/12} L^{-1/3} = c_3 (\epsilon \nu)^{1/4} \quad (19)$$

Now we turn to the shape function $\tilde{u}(x)$ of velocity profile. Since from the simulations we know the velocity profile can be well fit using polynomial up to 6th order, we propose phenomenologically

$$\tilde{u}(x) = 1 - 4u_2(x - 1/2)^2 - 16u_4(x - 1/2)^4 - 64u_6(x - 1/2)^6 \quad (20)$$

where the coefficients u_2, u_4, u_6 are functions of ϵ, g and L .

As expressed in Eq. (4), the 0th moment of $\tilde{u}(x)$ is characterized by γ . We find numerically that the scattered data of γ in Fig. 5 can be collapsed to one curve by using a combination of the dimensionless quantities P and Q : $Q^4/P = g^{1/2} L^{11/2} \epsilon / \nu^4$. Fig. 10 illustrates this point by plotting γ against $\Gamma = 10^{-5} g^{1/2} L^{11/2} \epsilon$ for the data of Fig. 5. We propose that the coefficients u_2, u_4, u_6 in Eq. (20) are functions of Γ and we determine their forms as follows.

Setting $x = 0$ in Eq. (20) and requiring $\tilde{u}(0) = \tilde{u}(1) = 0$, we know that u_2, u_4, u_6 are related by

$$u_2 + u_4 + u_6 = 1 \quad (21)$$

So we need only to determine u_2 and u_4 which must satisfy the following conditions:
(i) when $\epsilon = 0$, $u_2 = 1$, $u_4 = 0$ which recovers the parabolic velocity profile for fluids;
(ii) when $\epsilon \rightarrow \infty$, the velocity profile becomes completely flat and therefore $u_2 = 0$, $u_4 = 0$. We propose u_2 and u_4 as functions of Γ :

$$u_2 = \frac{1}{1 + d\Gamma} \quad (22)$$

$$u_4 = \frac{e\Gamma}{1 + h\Gamma^2} \quad (23)$$

where d, e, h are constants. Substituting the above expressions into Eq. (20) and integrating that equation we obtain

$$\begin{aligned} \gamma^{-1} &= \frac{90 - 20u_2 - 6u_4}{105} \\ &= \frac{90 - \frac{20}{1+d\Gamma} - \frac{6e\Gamma}{1+h\Gamma^2}}{105} \end{aligned} \quad (24)$$

We check the above expressions by fitting the numerical data of γ using Eq. (24). This is shown in Fig. 10. One sees that the fitting is very well except for γ close to 1.0 (corresponding to rather flat velocity profiles where $(x - 1/2)^8$ might be necessary in Eq. (20).).

Finally we make a remark that velocity profile such that $\tilde{u}(x) = 1 - u_\omega(x - 1/2)^\omega - 4u_2(x - 1/2)^2$ with $0 < \omega < 2$ is not in accord with γ shown in Fig. 5.

V. Discussions

In this paper we have numerically studied the granular flow in channels using a two-dimensional lattice gas automaton model. We have explored the dependences of velocity profile on dissipation, gravity and channel width and compared them with those of Newtonian fluids. Parabolic velocity profile is no longer valid as long as there is energy dissipation in the system. However, the deviation from parabolic profile depends on the degree of energy dissipation in a smooth way (there is no sharp

transition near $\epsilon = 0$). This may explain the fact that the experimental data of Savage [26] is close to a parabolic velocity profile, though he did not notice this point in his paper. However, the velocity profile can also be very flat depending on the dissipation and the channel width. The observation of Soo [27] confirms this point experimentally. Our results also show that the velocity profiles are more blunted than the parabolic form. We do not find any velocity profile that is sharper than parabolic shape (i.e., our γ are all less than 1.5), in contrast with Savage's theory [26] which predicted that profiles sharper than parabolic ones are possible to exist. The maximal velocity at the center is a linear function of gravity as $u_{max} = \alpha g - \delta$ but with non-zero δ . Here α behaves no longer as L^2 as for Newtonian fluids. Density profiles are no longer uniform but are higher near the boundaries than at the center. From the simulations we note that this nonuniformity is caused by the rest particles while the moving particles are distributed uniformly. This may have a link to the clustering of dissipative systems [44]. The boundaries which are represented by rough walls seem to serve as clustering seeds due to the non-slip boundary conditions we used. An earlier experiment by Soo [27] also showed that density increases toward the wall, as we find here. It is interesting to note that the recent experiment of Pouliquen and Gutfraind [45] showed that density near the wall is lower than that at the center. We attribute this contradiction with our numerical results to the different boundary conditions. In their experiments, considerable slip velocities were observed at the walls. Both increasing and decreasing density profiles toward the walls in different regimes were obtained theoretically in Ref. [28] and both kinds of experimental evidences were cited there.

In our model we find that the width of the region of higher densities (than the average density) relative to the channel width is a decreasing function of a variable which scales with the driving force (g), energy dissipation parameter (ϵ) and the width of the system (L) as $g^\mu L^\nu / \epsilon$ with exponents $\mu = 1.4 \pm 0.1$ and $\nu = 0.5 \pm 0.1$. Such a scaling was not found in any previous investigations. We have shown that $P = g^{3/2} L^{1/2} / \epsilon$ is a fundamental dimensionless parameter in the present system. Combined this with $Q = g^{1/2} L^{3/2} / \nu$, all of the results obtained in simulations have been successfully understood.

In this paper we have used non-slip boundary conditions at the channel walls. Unlike in viscous fluids, non-slip boundary conditions are not necessarily satisfied in every case of granular flow [46]. In fact, the general boundary conditions for granular flow is still lacking. However, as noted by Savage [26], the non-slip condition may be realized by providing wall roughness of the same order as that of the particle surface constituting the granular material, as he achieved in his experiments [26].

Acknowledgments

This work was supported by Grant-in-Aid of Ministry of Education, Science and Culture of Japan. G. P. thanks the Japan Society for the Promotion of Science for a postdoctoral fellowship.

References

- [1] J. C. Williams, Powder Technol.**15**, 245 (1976).
- [2] P. K. Haff and B. T. Werner, Powder Technol.**48**, 239 (1986).
- [3] A. Rosato, K. J. Strandburg, F. Prinz, and R. H. Swendsen, Phys. Rev. Lett. **49**, 59 (1987).
- [4] P. Devillard, J. Phys. France **51**, 369 (1990).
- [5] M. Faraday, Philos. Trans. R. Soc. London **52**, 299 (1831).
- [6] P. Evesque and J. Rajchenbach, Phys. Rev. Lett. **62**, 44(1989).
- [7] Y. H. Taguchi, Phys. Rev. Lett. **69**, 1367(1992).
- [8] J. A. C. Gallas, H. J. Herrmann, and S. Sokolowski, Phys. Rev. Lett. **69**, 1371(1992).
- [9] C-h. Liu and S. R. Nagel, Phys. Rev. Lett. **68**, 2301(1992).
- [10] H. M. Jaeger and S. R. Nagel, Science **255**, 1523(1992).
- [11] H. M. Jaeger and S. R. Nagel, and R. P. Behringer, Rev. Mod. Phys. **68**, 1259(1996); H. M. Jaeger and S. R. Nagel, and R. P. Behringer, Phys. Today **49**, 32(1996).
- [12] H. Hayakawa, H. Nishimori, S. Sasa, and Y.-h. Taguchi, Jpn. J. Appl. Phys. Part 1 **34**, 397(1995).
- [13] *Disorder and Granular Media*. edited by A. Hansen and D. Bideau (North-Holland, Amsterdam, 1992).
- [14] *Granular Matter*. edited by A. Mehta (Springer, Heidelberg, 1994).
- [15] K. L. Schick and A. A. Verveen, Nature **251**, 599(1974).
- [16] G. W. Baxter, R. P. Behringer, T. Fagert, and G. A. Johnson, Phys. Rev. Lett. **62**, 2825(1989).
- [17] T. Pöschel, J. Phys. I France, **4**, 499(1992).

- [18] G. Ristow and H. J. Herrmann, Phys. Rev. E **50**, R5(1994).
- [19] J. Lee, Phys. Rev. E **49**, 281(1994).
- [20] G. Peng and H. J. Herrmann, Phys. Rev. E **49**, R1796(1994); *ibid.* **51**, 1745(1995).
- [21] S. Horikawa, A. Nakahara, T. Nakayama, and M. Matsushita, J. Phys. Soc. Japan **64**, 1870(1995).
- [22] R. A. Bagnold, Proc. Roy. Soc. A **225**, 49(1954).
- [23] P. K. Haff, J. Fluid Mech. **134**, 401(1983).
- [24] J. T. Jenkins and S. B. Savage, J. Fluid Mech. **130**, 187(1983).
- [25] There is still controversy over the validity of granular hydrodynamics. See, e.g., Y. Du, H. Li, and L. P. Kadanoff, Phys. Rev. Lett. **74**, 1268(1995).
- [26] S. B. Savage, J. Fluid Mech. **92**, 53(1979).
- [27] S. L. Soo, G. J. Trezek, R. C. Dimick, and G. F. Hohnstreiter, Ind. Engng Chem. Fund. **3**, 98(1964). see also Ref. [28].
- [28] M. A. Goodman and S. C. Cowin, J. Fluid Mech. **45**, 321(1971).
- [29] C. S. Campbell and C. E. Brennen, J. Fluid Mech. **151**, 167(1985); P. A. Thompson and G. S. Grest, Phys. Rev. Lett. **67**, 1751(1991); D. M. Hanes and D. L. Inman, J. Fluid Mech. **150**, 357(1985); O. R. Walton and R. L. Braun, J. Rheol. **30**, 949(1986).
- [30] J. Lee and H. J. Herrmann, J. Phys. A **26**, 373(1993).
- [31] A. Rosato, K. J. Strandburg, F. Prinz and R. H. Swendsen, Phys. Rev. Lett. **58**, 1038(1987); A. D. Rosato, Y. Lan and D. T. Wang, Powder Technol. **66**, 149(1991).
- [32] H. Caram and D. C. Hong, Phys. Rev. Lett. **67**, 828(1991); M. Y Choi, D. C. Hong, and Y. W. Kim, Phys. Rev. E **47**, 137(1993); J. K. Rudra and D. C. Hong, *ibid.* **47**, R1459(1993).

- [33] S. Luding, E. Clément, A. Blumen, J. Rajchenbach and J. Duran, Phys. Rev. E **49**, 1634(1994).
- [34] G. W. Baxter and R. P. Behringer, Phys. Rev. A **42**, 1017(1990); Physica D **51**, 465(1991).
- [35] M. P. Allen and D. J. Tildesley, *Computer Simulations of Liquids*, Clarendon Press, Oxford (1987).
- [36] H. J. Herrmann, Physica A **191**, 263(1993); in *Proceedings of the III Granada School*, Lecture Notes in Physics Vol. 448 (Springer, Berlin, 1994).
- [37] U. Frisch, B. Hasslacher, and Y. Pomeau, Phys. Rev. Lett. **56**, 1505(1986).
- [38] L. P. Kadanoff, G. R. McNamara, and G. Zanetti, Phys. Rev. E **40**, 4527(1989).
- [39] K. Balasubramanian, F. Hayot, and W. F. Saam, Phys. Rev. E **36**, 2248(1987).
- [40] D. H. Rothman and S. Zaleski, Rev. Mod. Phys. **66**, 1417(1994).
- [41] J. J. Alonso and H. J. Herrmann, Phys. Rev. Lett. **76**, 4911(1996).
- [42] A. Károlyi and J. Kertész, in *Proceedings of the 6th Joint EPS-APS International Conference on Physics Computing* (European Physics Society, Geneva, Switzerland, 1994).
- [43] S. Vollmar and H. J. Herrmann, Physica A **215**, 411(1995).
- [44] I. Goldhirsch and G. Zanetti, Phys. Rev. Lett. **70**, 1619(1993); S. McNamara and W. R. Young, Phys. Fluids A **5**, 34(1993).
- [45] O. Pouliquen and R. Gutfraind, Phys. Rev. E **53**, 552(1996).
- [46] E. E. Ehrichs, H. M. Jaeger, G. S. Karczmar, J. B. Knight, V. Y. Kuperman, and S. R. Nagel, Science **267**, 1632(1995).

Figure Captions

Figure 1: (a) Sketch of the two-dimensional triangle lattice. Gravity is along y -direction. One complete hexagon is drawn; (b) Probabilistic collision rules for two- and three-body collisions. Thin arrows represent particles and small circles stand for rest particles. The number next to a configuration is the probability that the configuration takes place; (c) Collision rules for moving particles with a rest particle. Immediately after the collision, more than one rest particle on a site will hop to the nearest neighbouring sites randomly until they find a suitable site with no rest particle already there.

Figure 2: Total kinetic energy E versus time step by running the LGA starting from a random initial configuration. The kinetic energy of a moving particle is taken to be a unit. The plotted curve was obtained with $\epsilon = 0.01$. The total momentum added to the system each time is $G = 7.0$, channel width $L = 64$ and average density $\bar{\rho} = 1.5$.

Figure 3: (a) Velocity profile for the LGA with ϵ set to zero. Here the total momentum added to the system each time is $G = 1.0$, channel width $L = 64$ and average density $\bar{\rho} = 1.8$. The curve is the best (least-square) fit to the numerical data using a polynomial fitting routine up to second order; (b) Density profile corresponding to (a).

Figure 4: (a) Velocity profile for the LGA with $\epsilon = 0.01$. Here the total momentum added to the system each time is $G = 7.0$, channel width $L = 64$ and average density $\bar{\rho} = 1.5$. The upper curve is the best (least-square) fit to the numerical data using a polynomial fitting routine up to second order and the lower curve is a parabolic curve by demanding the maximal value at the center equal to the numerical data and zero at the two boundaries; (b) Density profile corresponding to (a).

Figure 5: The ratio $\gamma = u_{max}/\bar{u}$ versus gravity g for different channel widths $L = 32, 48, 64, 128$ (from top to bottom) with $\epsilon = 0.01$ (data points connected by solid lines) and $\epsilon = 0.02$ (data points connected by dashed lines).

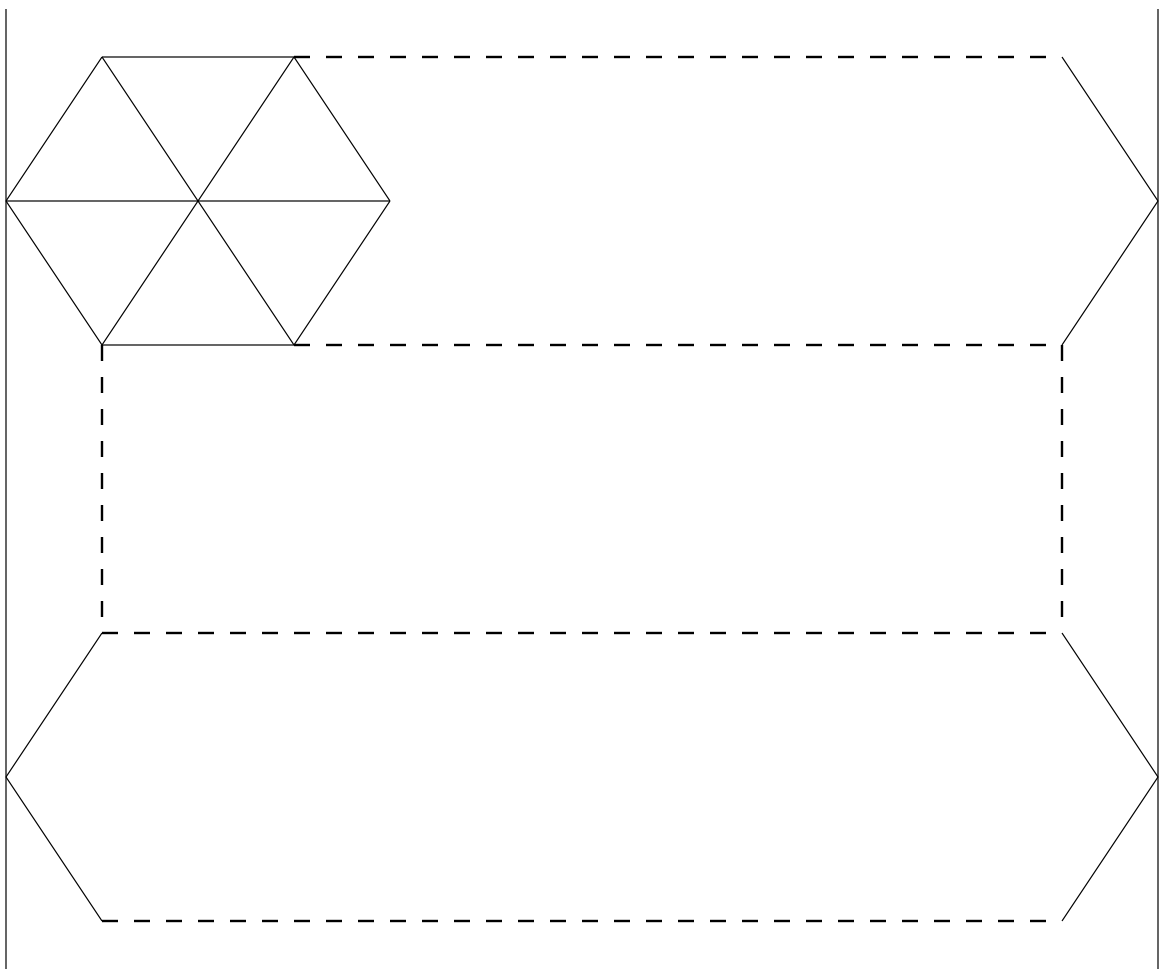
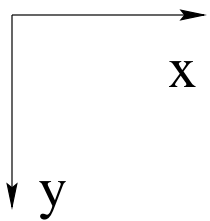
Figure 6: The normalized shape function $\tilde{u}(x)$ as a function of x in the interval $[0:1]$. Two curves corresponding to $\{\epsilon = 0.02, L = 48, G = 10.0(g = 0.00434028)\}$ (\diamond) and $\{\epsilon = 0.01, L = 64, G = 8.0(g = 0.00195312)\}$ (+) are almost identical, though the two set parameters share no common value. Another curve (\square) corresponding to $\{\epsilon = 0.02, L = 48, G = 5.0(g = 0.00217014)\}$ is shown for comparison. This curve shares two parameters ϵ and L with the curve (\diamond) but their difference is obvious. Lines are best fit to the numerical data using a polynomial fitting routine up to 6th order as expressed in Eq. (5). The fitting parameters are $\{v_0 = 0.999664, v_2 = 1.25789, v_4 = -0.51635, v_6 = 53.8739, c = 0.493339\}$ (\diamond), $\{v_0 = 0.998367, v_2 = 1.35365, v_4 = -1.83773, v_6 = 55.4401, c = 0.494999\}$ (+) and $\{v_0 = 0.997691, v_2 = 1.81431, v_4 = 4.97792, v_6 = 20.8538, c = 0.493152\}$ (\square).

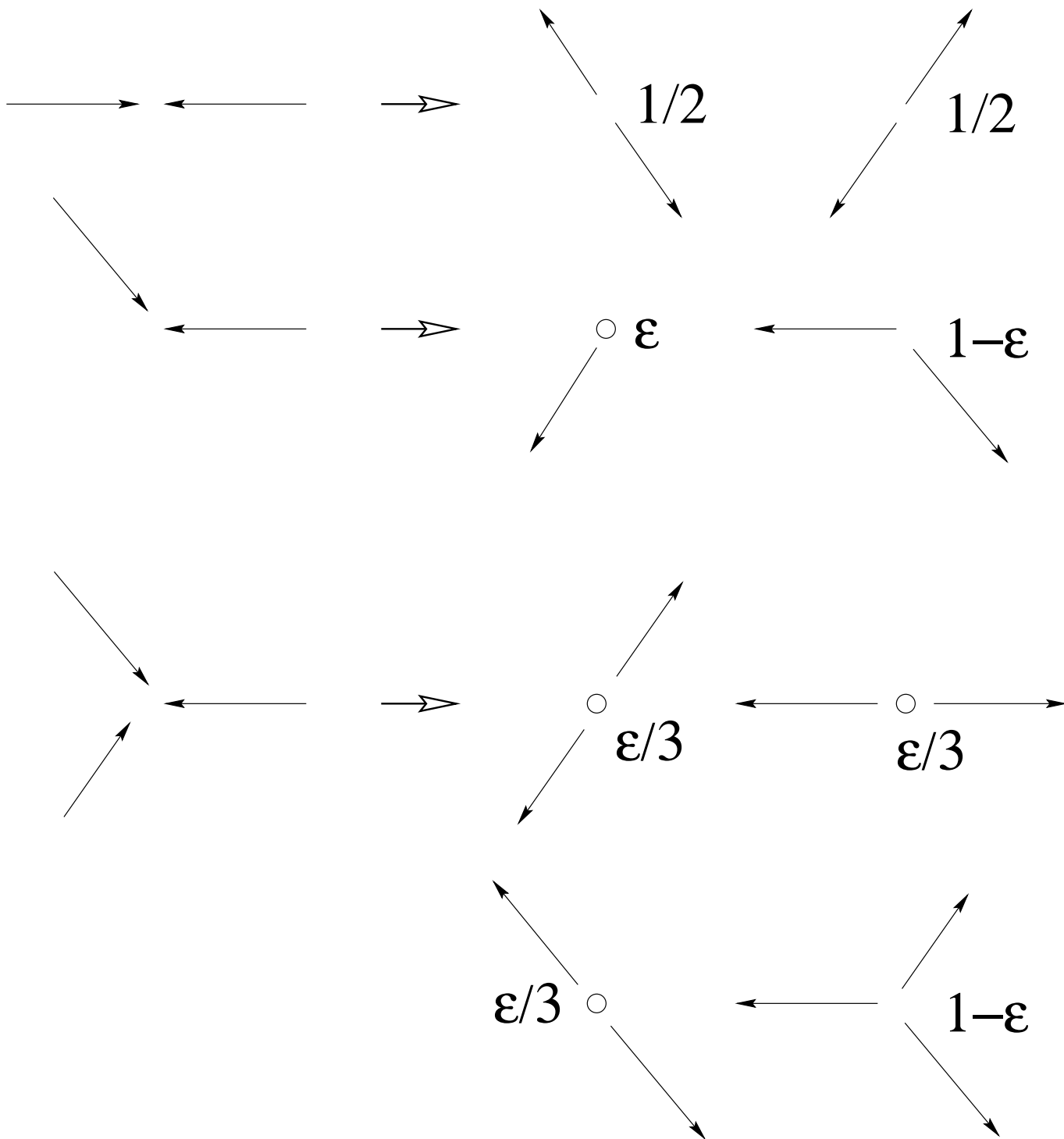
Figure 7: u_{max} versus gravity g for four different channel widths $L = 32, 48, 64, 128$ (from bottom to top) and for $\epsilon = 0.02$. The lines are least-squares linear fit to the numerical data. Four lines cut the vertical axis at non-zero positions which are very close to each other.

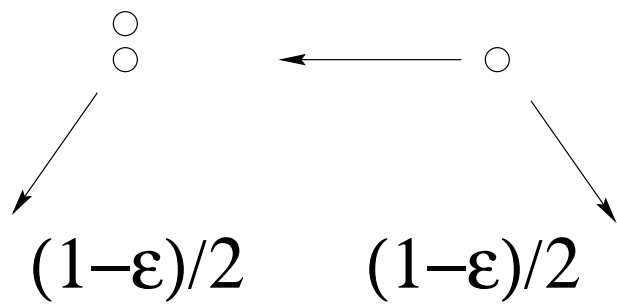
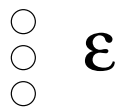
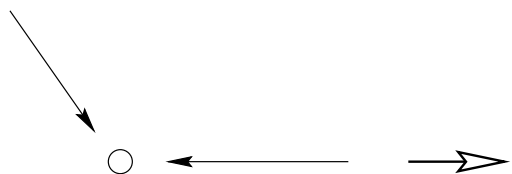
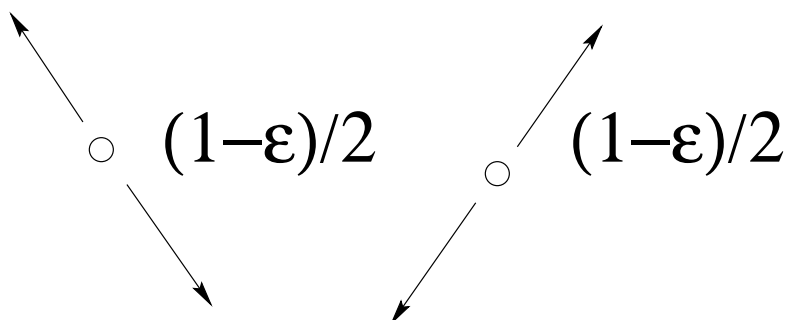
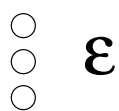
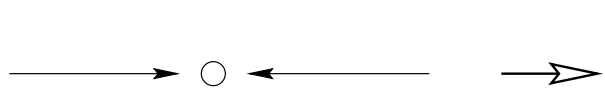
Figure 8: (a) The width of higher densities (than average density) relative to the channel width Δ/L are plotted versus the gravity g for different channel widths and different dissipation parameters. A: $\{\epsilon = 0.01, L = 32\}$, B: $\{\epsilon = 0.01, L = 128\}$, C: $\{\epsilon = 0.02, L = 48\}$, D: $\{\epsilon = 0.02, L = 64\}$, E: $\{\epsilon = 0.02, L = 128\}$, F: $\{\epsilon = 0.04, L = 48\}$, G: $\{\epsilon = 0.04, L = 64\}$. (b) Data collapse of (a): Δ/L are plotted versus $g^\mu L^\nu / \epsilon$ with $\mu = 1.4$ and $\nu = 0.5$.

Figure 9: α versus $L^{2/3}$ for $\epsilon = 0.01$ (\diamond) and $\epsilon = 0.02$ (+).

Figure 10: Data collapse of Fig. 5: γ versus $\Gamma = 10^{-5}g^{1/2}L^{11/2}\epsilon$. Symbols are the same as those in Fig. 5. Solid line is the best fit to the numerical data using Eq. (24). The logarithm of horizontal axis is made for clarity of displaying data. The fitting parameters in Eq. (24) are $d = 0.0097748$, $e = -0.350605$ and $h = 0.00268941$.







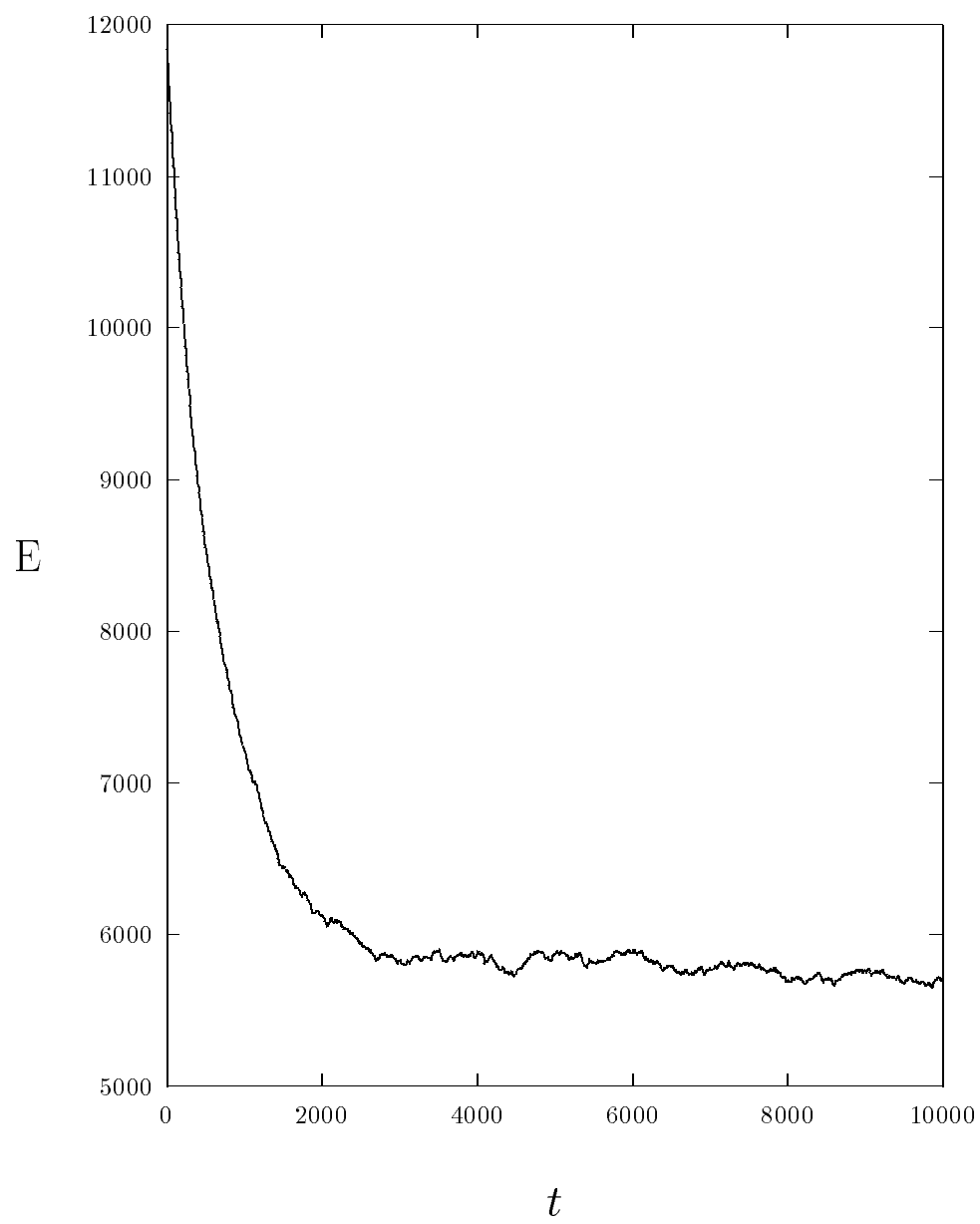


Fig. 2 –Peng and Ohta

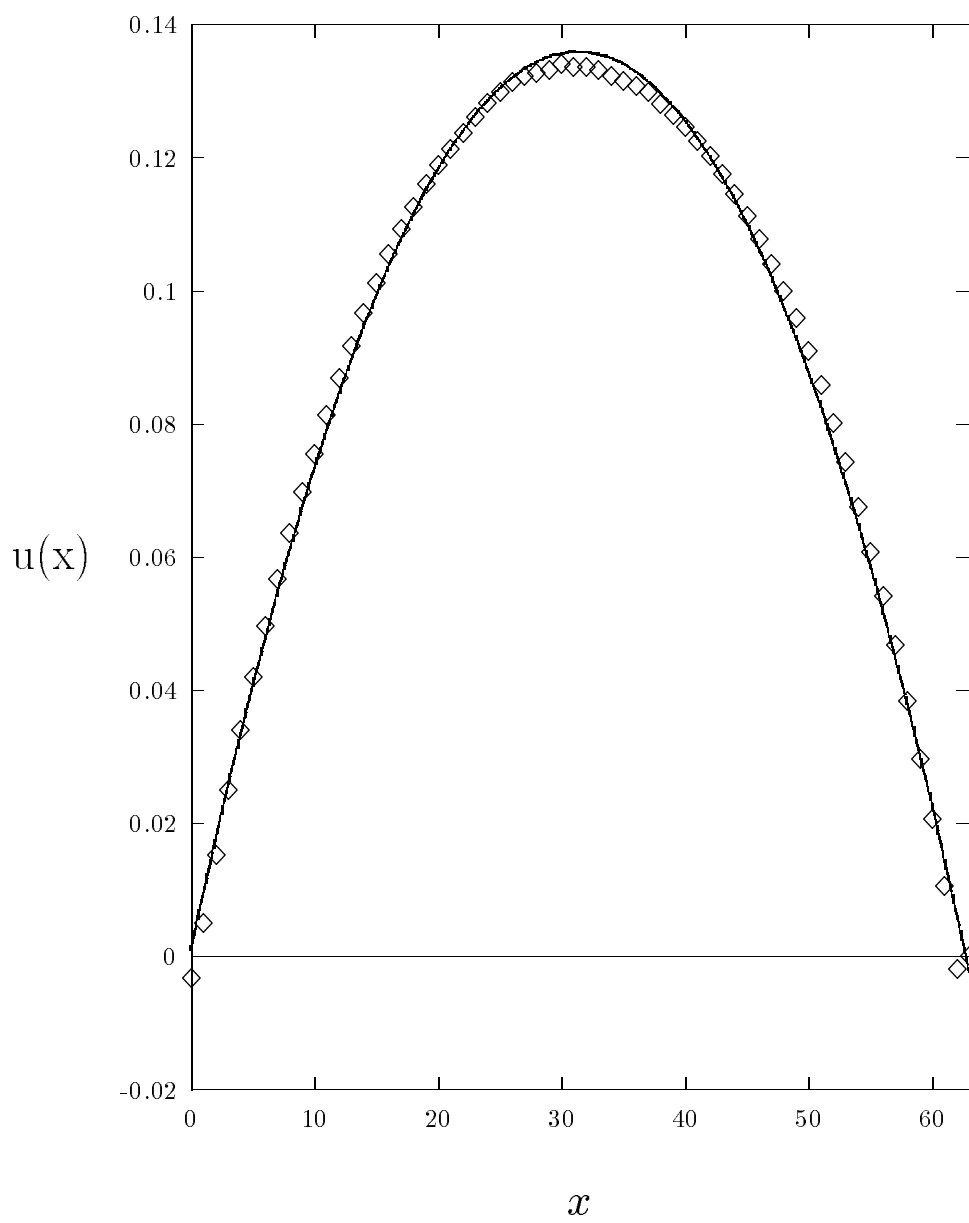


Fig. 3a –Peng and Ohta

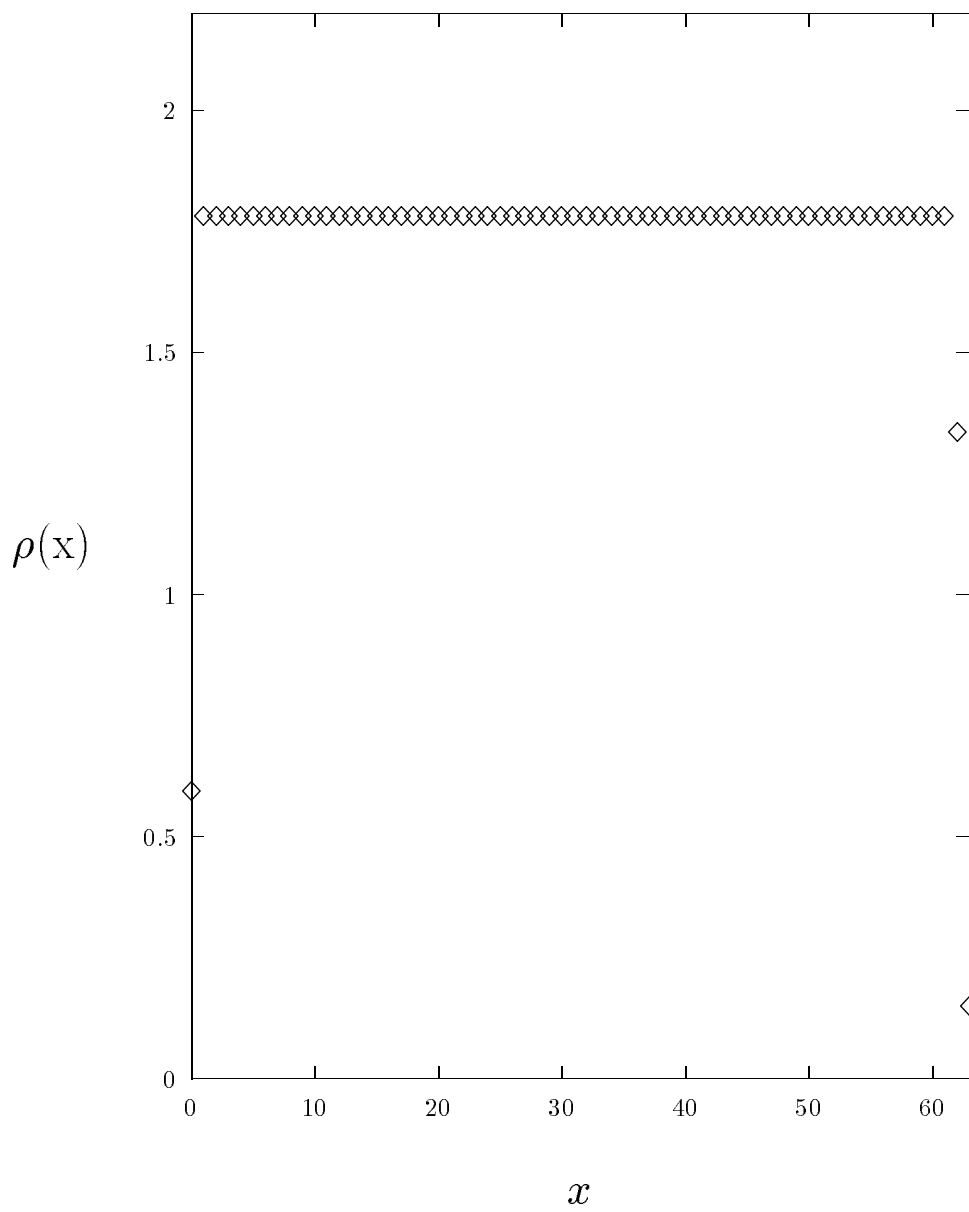


Fig. 3b –Peng and Ohta

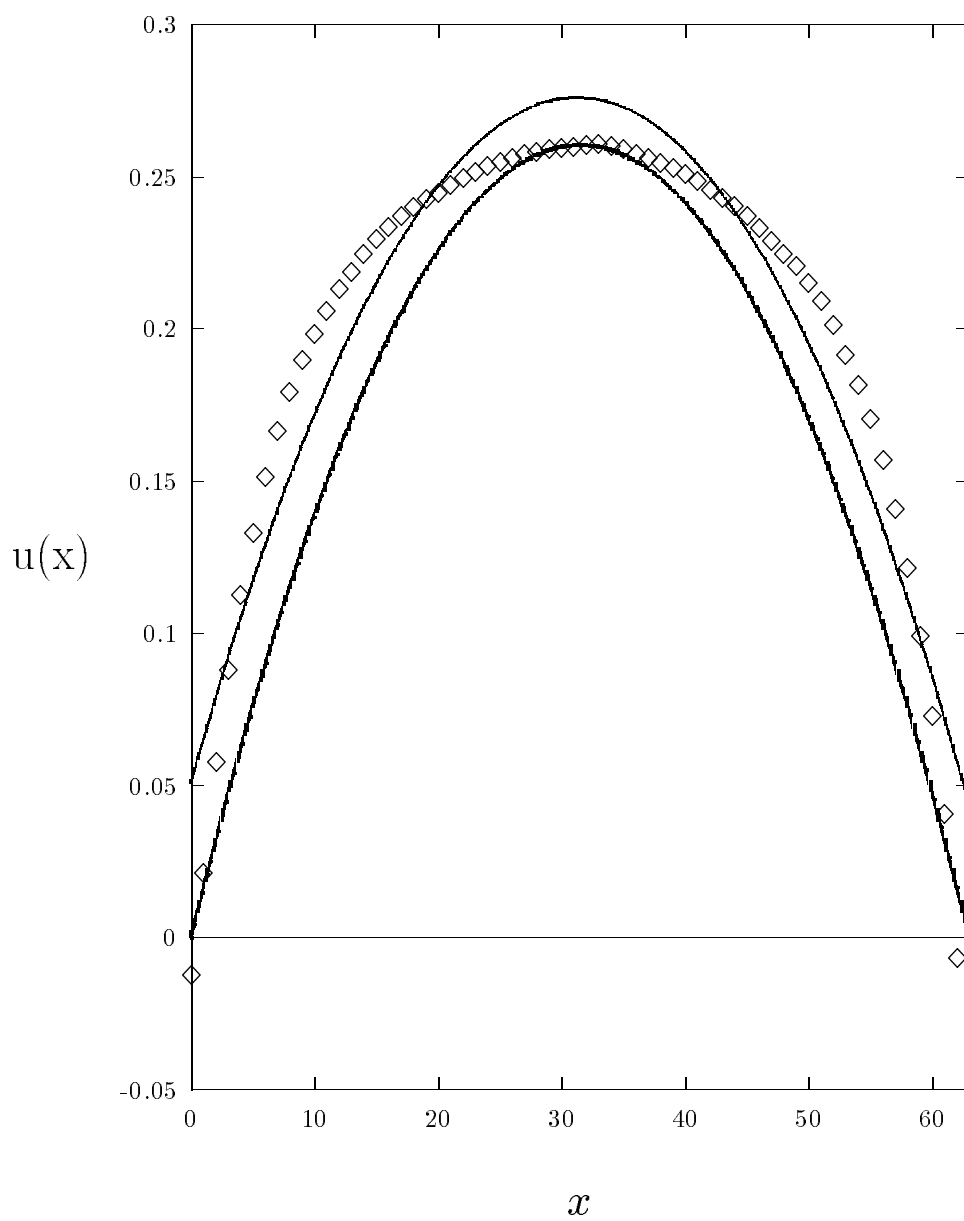


Fig. 4a –Peng and Ohta

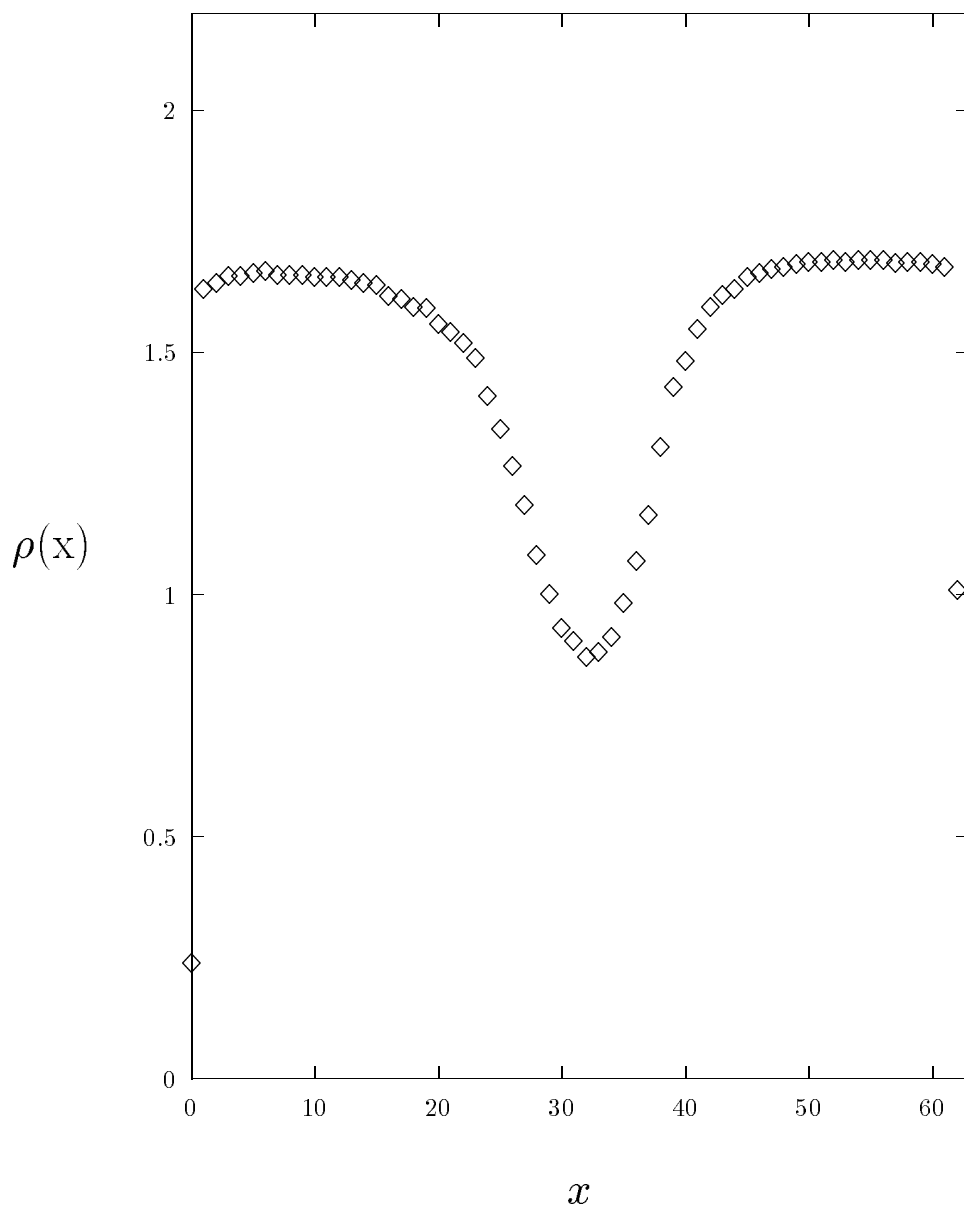


Fig. 4b –Peng and Ohta

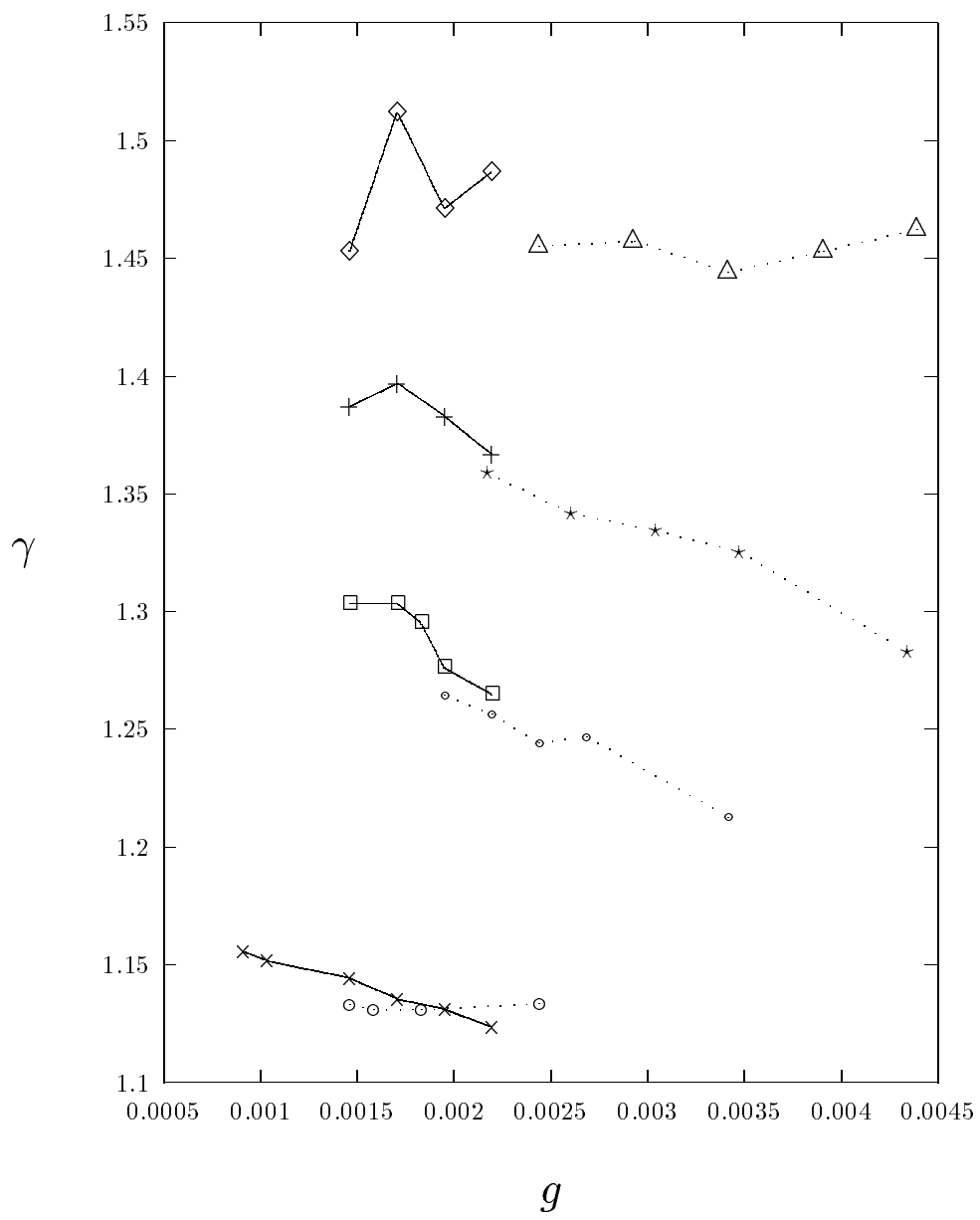


Fig. 5 –Peng and Ohta

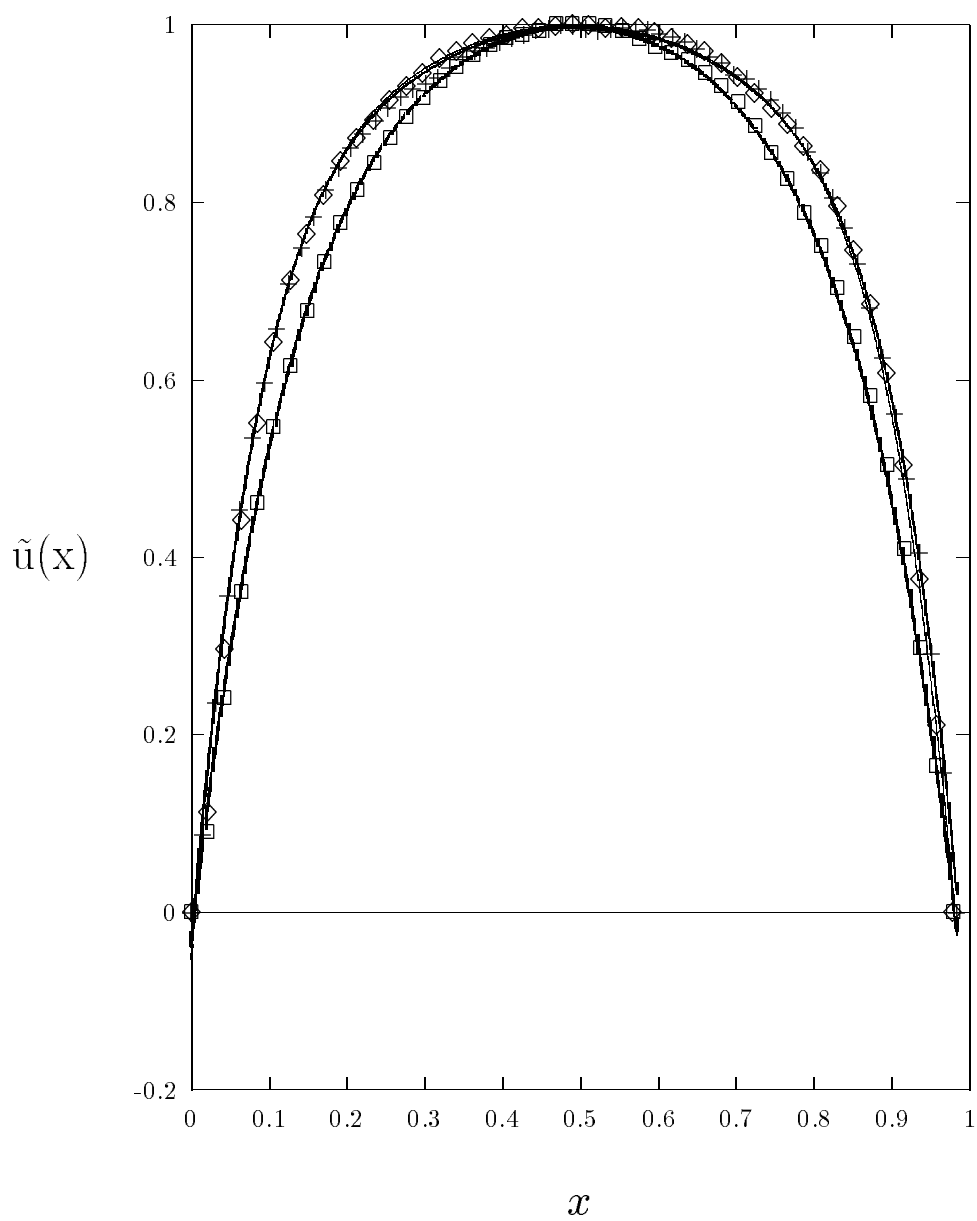


Fig. 6 –Peng and Ohta

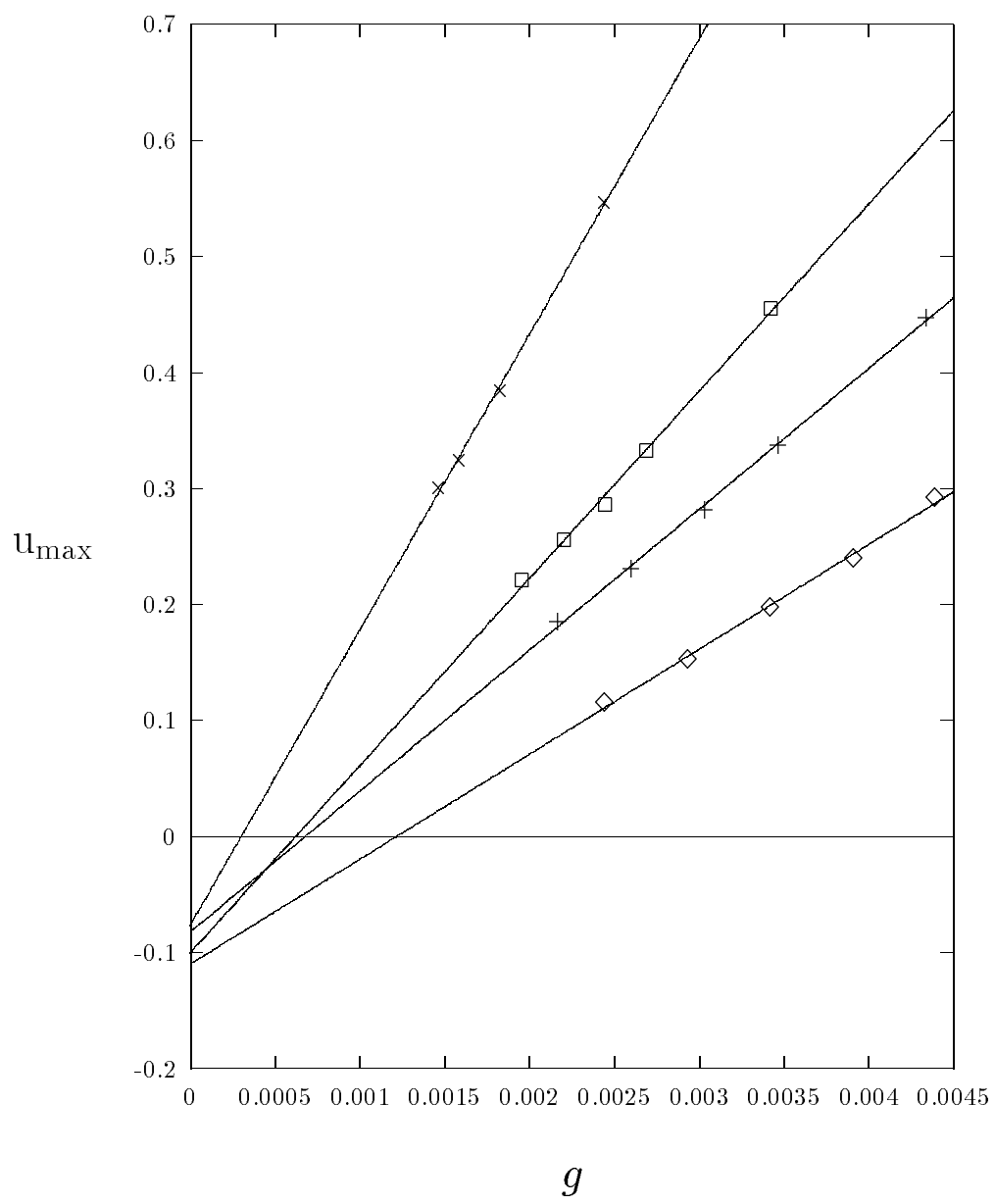


Fig. 7 –Peng and Ohta

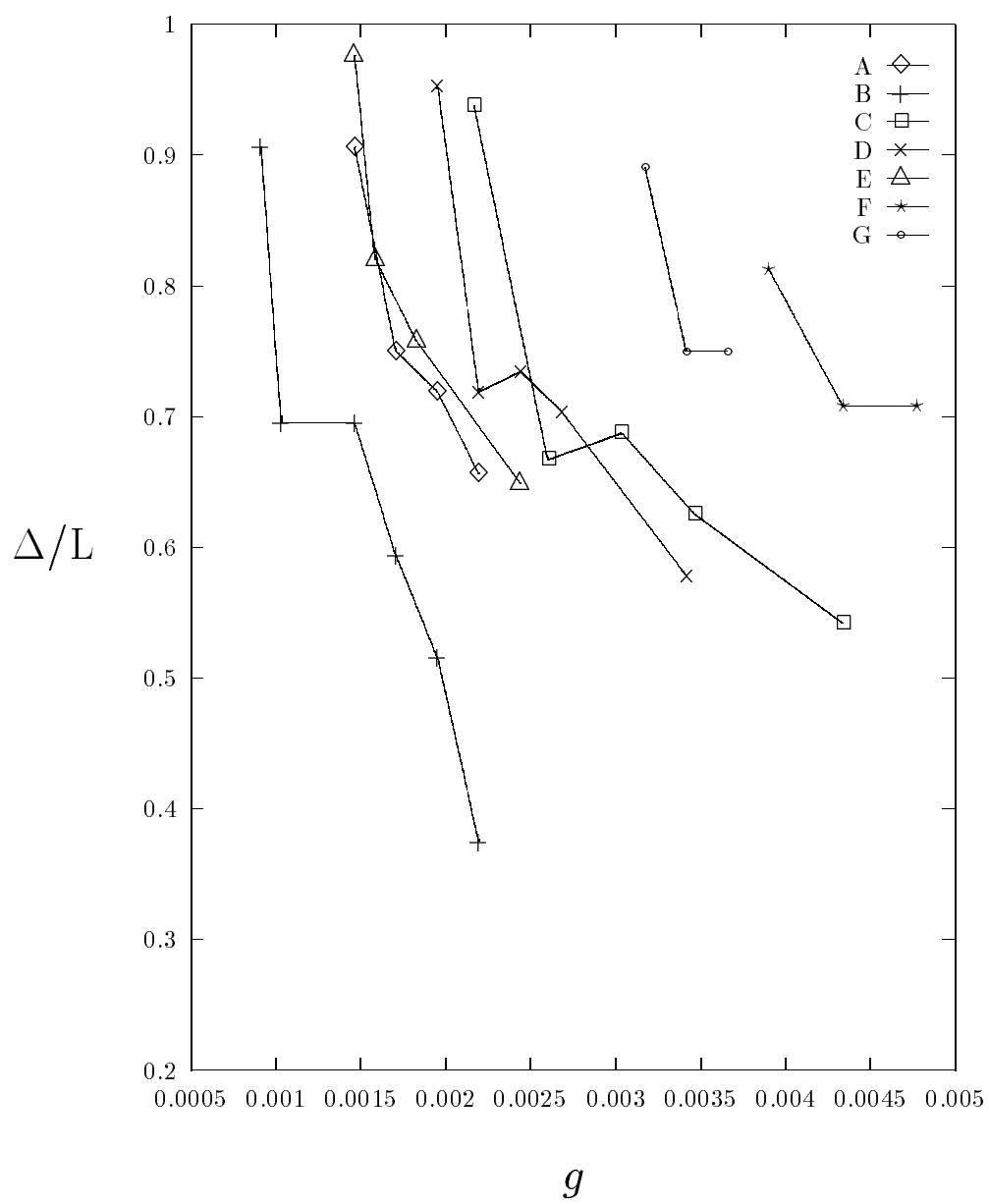


Fig. 8a –Peng and Ohta

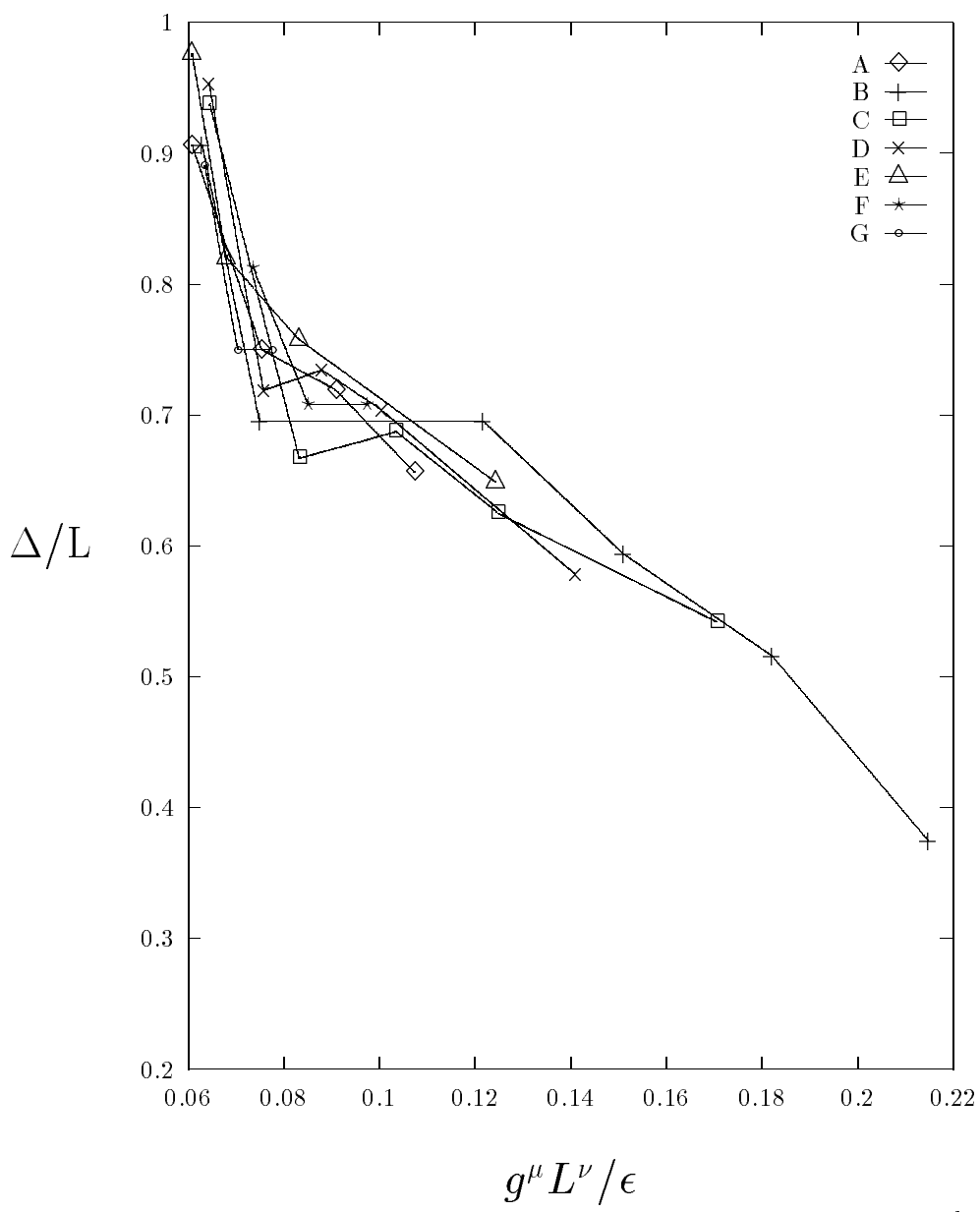


Fig. 8b –Peng and Ohta

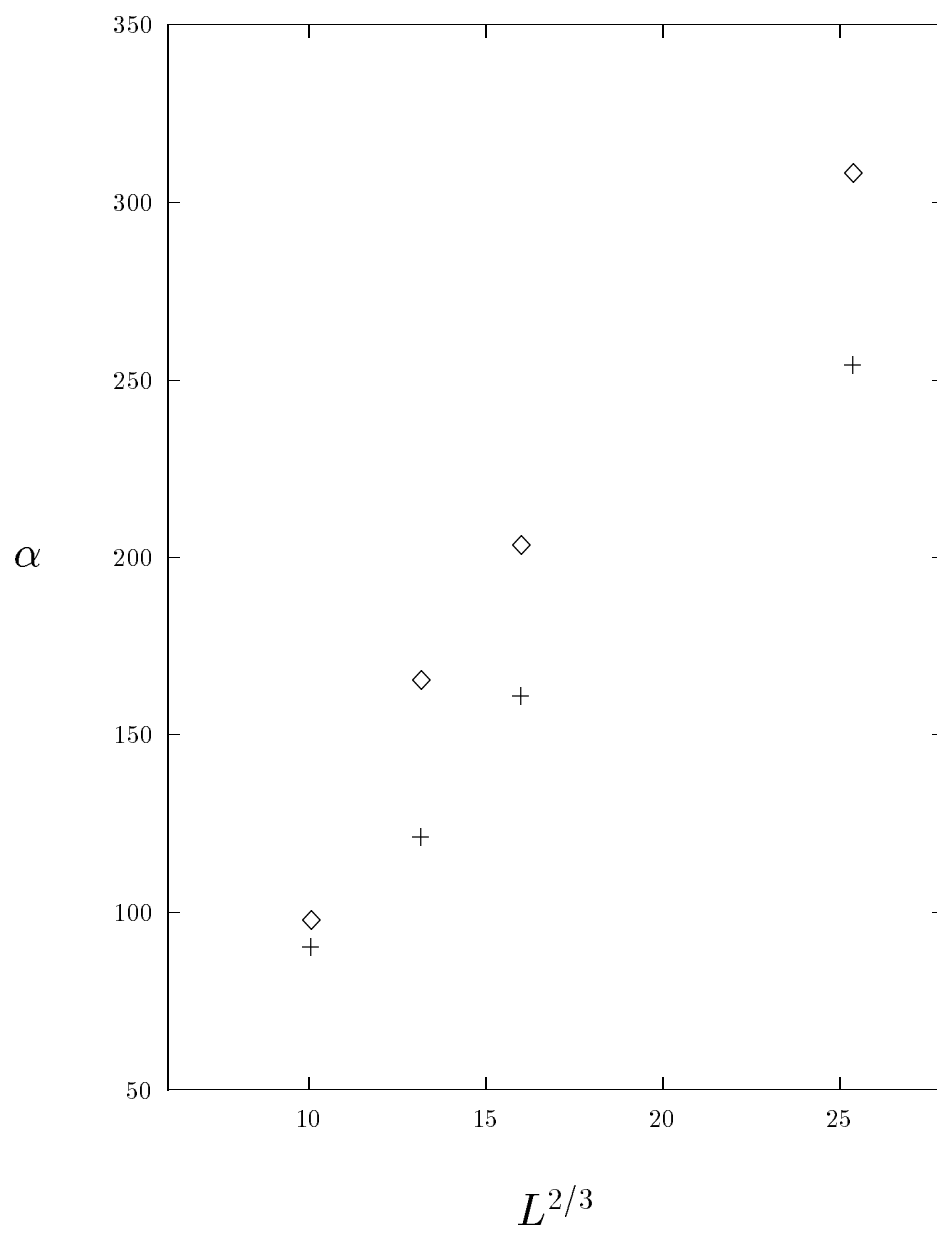


Fig. 9 –Peng and Ohta

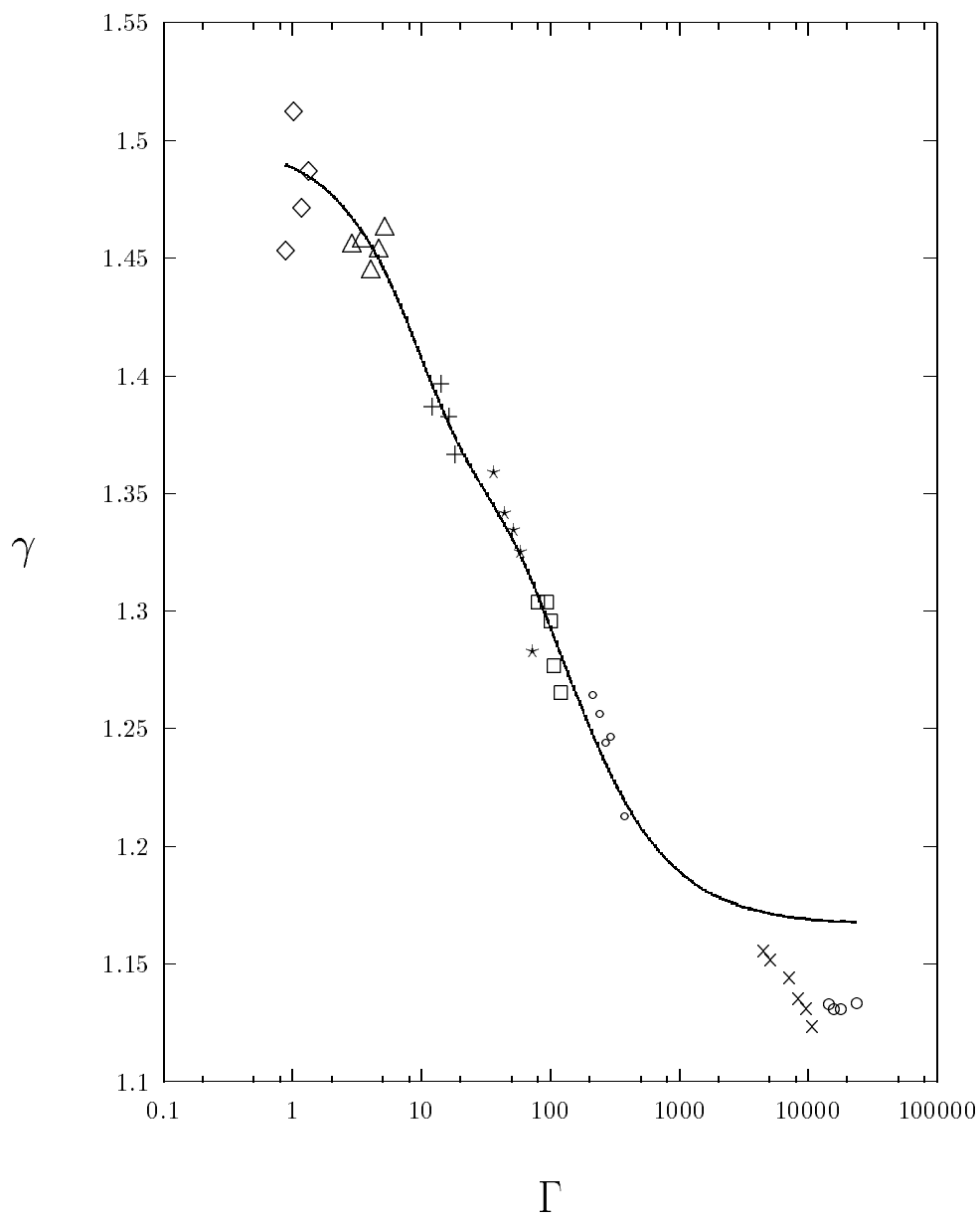


Fig. 10 –Peng and Ohta